The Near-Surface Current Velocity Determined from Image Sequences of the Sea Surface

Christian M. Senet, Jörg Seemann, and Friedwart Ziemer

***Abstract*—A method to measure the ocean's near-surface current velocity vector based on the analysis of remote sea-surface image sequences was developed. The spatial and temporal records were transformed to the wavenumber-frequency domain, resulting in a three-dimensional (3-D) image power spectrum. In the spectrum, the signal energy of the waves is localized on a shell defined by the dispersion relation of surface waves. The sum of the sensor's velocity and the near-surface current profile deforms the dispersion shell due to the Doppler-frequency shift. An iterative least-squares fitting technique and an error-estimation model was implemented. To improve the method's accuracy, spectral wave energy found in higher harmonics of the dispersion shell and aliasing effects are taken into account. The most important nonlinear mechanism leading to higher harmonics is explained as resulting from wave shadowing due to the low grazing angles typical for ground- or ship-based radars. The low rotation time of nautical radar antennas causes temporal undersampling, which leads to aliasing in the frequency domain. In this paper, the improved method is examined analytically and is tested with Monte Carlo simulations. The variation of the shape of the measured or simulated 3-D image spectra, especially the peak wavenumber, the directional spread, and the main travel direction, controls the behavior and accuracy of the technique. A comparison of velocities acquired by nautical radar and independent Doppler Log current measurements is presented. The technique's accuracy, its limits, and its adaptability are discussed. Additional improvements are proposed, which lead to higher accuracy considering the shape of the spectral background noise and the technique's applicability to high ship speeds. The presented method is an important step toward operationalization of a commercial wave-monitoring system based on nautical radars.**

***Index Terms*—Aliasing, coast, current, image-sequence analysis, least-squares, nonlinearity, ocean surface, operationalization, optics, radar, remote sensing, ship, wavenumber-frequency spectrum.**

I. INTRODUCTION

IMAGES of a nautical radar include sea-state information. Electromagnetic microwaves are backscattered by the small-scale roughness of the sea surface. This radar backscatter is modulated by long surface gravity waves. This phenomenon is called *sea clutter* [1]. A nautical radar measures in space x and y and time t. This instrument therefore is suitable to measure the spatial and temporal evolution of the sea-surface wave field $\zeta(x, y, t)$.

The wave monitoring system (WaMoS) has been developed at GKSS, Geesthacht, Germany, [2], [3] and is now an operationally used instrument [4], [5]. The system provides digitized time series of sea-clutter images. The spatial and temporal

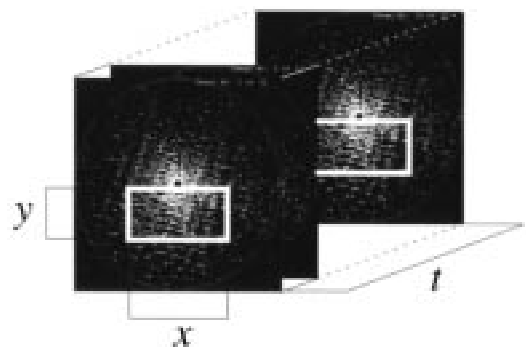

Fig. 1. Illustration of a time series of nautical radar images in the spatial and temporal domain. In the operational mode, the area selected for analysis (indicated by the white boxes) has a spatial size of $x = 2560$ m and $y = 1280$ m and a temporal size of 75.8 s.

sea-state information is stored as a image sequence cube of gray values $I(x, y, t)$ (see Fig. 1). A three-dimensional fast Fourier transformation (3-D FFT) is used to transform the spatio-temporal information into the spectral wavenumber-frequency domain Ω

$$|\mathrm{FFT}(I(x, y, t))|^2 = P(k_x, k_y, \omega) \tag{1}$$

where $k_x = 2\pi x^{-1}$ and $k_y = 2\pi y^{-1}$ are the components of the wavenumber vector $\vec{k}$, and $\omega = 2\pi t^{-1}$ is the angular frequency. The result of (1) is a 3-D image power spectrum $P(k_x, k_y, \omega)$. The spectral energy (or gray-level variance) of the imaged surface waves is located on a surface in the Ω-domain defined by the dispersion relation of surface gravity waves. This surface is called a dispersion shell. The dispersion shell is deformed by the relative movement between the sensor and the sea surface due to the Doppler effect. The relative movement is a superposition of the near-surface current velocity and the sensor's velocity relative to the ground. If the relative velocity or velocity of encounter $\vec{u}_e$ is known, the dispersion relation is used to locate spectral energy belonging to the surface waves and therefore can be used as a filter to separate this spectral part from the background noise. The spectral background noise originates from speckle (see [6]).

The determination of the velocity of encounter is a precondition to the integration of the sea-state signal over the positive frequencies, which allows the calculation of low-noise and unambiguous directional spectra, $P(k_x, k_y)$ [7], [8]. Therefore, the improvement of the algorithm's accuracy and the introduction of an error model to determine that accuracy is an important step toward the operationalization of WaMoS II. An empirical calibration procedure to determine the significant wave height

Manuscript received May 18. 1999; revised June 26, 2000.

The authors are with the Institute of Hydrophysics, GKSS Research Center, 21502 Geesthacht, Germany (e-mail: senet@gkss.de).

Publisher Item Identifier S 0196-2892(01)01171-8.

using buoy data for comparison with radar data has been developed based on the assumption that the SNR of the radar spectra correlates with the significant wave height, which is also well known from synthetic aperture radar (SAR) image spectra [9]. After calibration, WaMoS II yields fully directional spectra and significant wave height in real time [10]. Another application of WaMoS II is the determination of the wind velocity vector based on the directional and magnitudinal dependence of the spectral background noise on the wind field [11].

An algorithm based on a least-squares method (LSM) proposed by Young *et al.* [12] has been improved recently. The improvements are as follows: 1) the consideration of nonlinear spectral structures to increase the number of regression coordinates and therefore also increase the accuracy significantly, and 2) the application of a spectral refolding technique to allow the correction of temporal undersampling (aliasing) due to the slow rotation time of a nautical radar antenna. The latter increases the number of regression coordinates as well. The improved algorithm, consisting of a linear regression and an error model, will be presented here. To examine the response of the algorithm to variations of the wave field, Monte Carlo simulations of nautical radar image sequences and analytical examinations are performed to test the algorithm. Accordingly, a comparison of ship-based radar measurements and Doppler Log current measurements are presented and discussed. Thus, for the first time, the method is validated with an independent current sensor. Furthermore, it will be shown with land-based radar measurements that a typical temporal evolution of a coastal tidal current is reproduced qualitatively. For this case no comparable data sets have been acquired. The application of the algorithm to optical image sequences is discussed briefly.

II. VELOCITY OF ENCOUNTER

In this section, the measured quantity is introduced and the principle of the method by which it is determined is given. In addition, an error model to describe the accuracy of determination is presented.

A. Definition

The velocity of encounter $\vec{u}_e$ is the vector sum of the platform's (i.e., a ship) velocity $\vec{u}_s$ and the near-surface current velocity $\vec{u}_c(z)$, where z is the vertical coordinate. The accuracy of the near-surface current velocity measured by a radar depends on the actual sea state (frequency-shifted by the Doppler effect) since the imaged wave field is the carrier of the velocity information. The Doppler-frequency shift is induced by the near-surface current down to the penetration depth of the waves. The penetration depth for a single wave is approximately half of its wavelength $h_\lambda = \lambda/2$. Stewart and Joy [13] have shown that the component of the velocity of encounter $\vec{u}_e$ in the direction of the wavenumber vector $\vec{k}$ is a weighted mean current over the upper layer of the ocean. This result has been extended [12] to consider the full current vector

$$\vec{u}_e(z) = 2k \int_{-d}^{0} \vec{u}(z)_c e^{(2kz)}\, dz \tag{2}$$

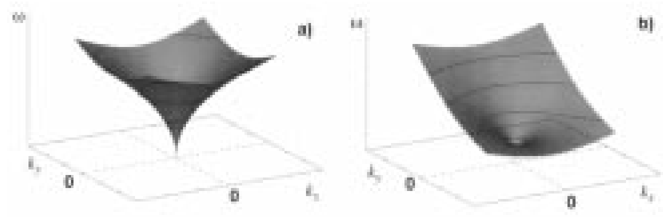

Fig. 2. (a) Intrinsic and (b) Doppler-shifted dispersion shell in the Ω-domain.

where $\vec{u}_c(z)$ is the vertical velocity vector profile. This definition is for a single wave. The extension of (2) to a wave field (assumed to be a superposition of waves) is given in Section IV.

B. Determination

The method used to determine the velocity of encounter is based on an adaptation of the dispersion relation of sea-surface gravity waves to the wavenumber components k_x and k_y and frequency coordinates ω of the sea-state signal found in the spectrum $P(k_x, k_y, \omega)$. This adaptation was realized with a least-squares regression method.

In the Ω-domain, a curved plane described by the dispersion relation of linear gravity waves is defined

$$\varsigma^2(k) = gk\ \tanh(kh) \tag{3}$$

where

- ς intrinsic frequency;
- g acceleration due to gravity;
- k modulus of the two-dimensional (2-D) wavenumber vector $|\vec{k}|$;
- h water depth.

The dispersion relation (3) is valid when the sensor velocity and the near-surface currents are zero.

The so-called *dispersion shell* (3) is illustrated in Fig. 2(a). Imaging of surface waves by nautical radar is nonlinear. The linear part, described by an image transfer function (ITF), results in spectral energy, which is localized on the dispersion shell. The impact of the Doppler term ω_D added to the intrinsic frequency ς is illustrated in Fig. 2(b) and is described as

$$\mathcal{S}\left(\vec{k}, \vec{u}_e\right) = \varsigma + \omega_0 \tag{4}$$

where

$$\omega_0 = ku_e\ \cos(\theta) \tag{5}$$

is the frequency of encounter (or the absolute frequency), and θ is the angle between $\vec{k}$ and $\vec{u}_e$. The dependency on the cosine function of ω_D implies that only the component of $\vec{u}_e$ parallel to the wave's travel direction given by the wavenumber vector $\vec{k}$ effects the Doppler-frequency shift. The Doppler term $\omega_D = ku_e\ \cos(\theta)$ in (4) can be written in Cartesian coordinates as follows:

$$\omega_D\left(\vec{k}, \vec{u}_e\right) = k_x u_x + k_y u_y. \tag{6}$$

The minimum criterion

$$Q^2 = \sum_{i=1}^{N} \left(\frac{\omega_i - \mathcal{S}\left(\vec{k}_i\right)}{\sigma_\omega} \right)^2 \Rightarrow \min \tag{7}$$

leads to a linear system of two equations

$$\begin{aligned} \partial Q^2/\partial u_x &= 0 \\ \partial Q^2/\partial u_y &= 0 \end{aligned} \tag{8}$$

where

u_x and u_y components of the velocity of encounter;
N number of coordinates collected for the LSM;
σ_ω expected standard deviation of the error difference.

$$\omega_{D,i} = \omega_i - \mathcal{S}\left(\vec{k}_i\right) \tag{9}$$

where ω_i is the ith frequency component of a selected regression coordinate found in $P(k_x, k_y, \omega)$, and $\mathcal{S}(\vec{k}_i)$ is the theoretical frequency value calculated with $\vec{k}_i$ following (4).

The standard deviation must be estimated (see Section II-C). The equation system in matrix notation is given as

$$\begin{pmatrix} \mathcal{D}_{xx} & \mathcal{D}_{xy} \\ \mathcal{D}_{yx} & \mathcal{D}_{yy} \end{pmatrix} \begin{pmatrix} u_x \\ u_y \end{pmatrix} = \begin{pmatrix} b_x \\ b_y \end{pmatrix} \tag{10}$$

or in the abbreviated form

$$D\vec{u} = \vec{b}. \tag{11}$$

The coefficients of matrix D in (10) and (11) are

$$\mathcal{D}_{xx} = \sum_{i=1}^{N} \frac{k_{x,i}^2}{\sigma_\omega^2}, \quad \mathcal{D}_{xy} = \mathcal{D}_{yx} = \sum_{i=1}^{N} \frac{k_{x,i} k_{y,i}}{\sigma_\omega^2}$$

and

$$\mathcal{D}_{yy} = \sum_{i=1}^{N} \frac{k_{y,i}^2}{\sigma_\omega^2}. \tag{12}$$

The components of the vector $\vec{b}$ are

$$b_x = \sum_{i=1}^{N} \frac{k_{x,i}\omega_{D,i}}{\sigma_\omega^2} \quad \text{and} \quad b_y = \sum_{i=1}^{N} \frac{k_{y,i}\omega_{D,i}}{\sigma_\omega^2}. \tag{13}$$

To determine the unknowns u_x and u_y (which are the components of the velocity of encounter $\vec{u}_e$), the matrix D must be invertible [i.e., $\det(D) \neq 0$]. If matrix D is invertible, the solution vector $\vec{u}_e$ is given by $D^{-1} \cdot \vec{b}$.

C. Error Estimation Model

Here, an error model for the determination of the velocity of encounter is introduced. The calculated velocity of encounter $\vec{u}_e$ is assumed to be the most likely vector of the "true" vector $\vec{u}_{e,T}$. The difference vector $\vec{u}_{e,T} - \vec{u}_e$ is defined as the absolute error. *A priori*, the absolute error is unknown. An assumption for the accuracy is only given as a probability. For the 2-D vector $\vec{u}_e = (u_x, u_y)$, a two-dimensional (2-D) probability is represented by a confidence ellipse. This confidence ellipse is represented by the length of the ellipse's half axes a and b and the ellipse's orientation angle θ.

The error model is based on the assumption that the frequencies of encounter $\mathcal{S}(\vec{k}_i)$ follow a Gaussian distribution around the discrete frequency bins ω_i ($\Delta\omega$ is limited due to the finite measurement duration, e.g., spectral leakage). With this assumption, the values of Q^2 are χ^2_ν-distributed. The number of degrees of freedom ν are given by $\nu = N - 2$; the number of spectral regression coordinates N reduced by the number of regression parameters (u_x, u_y). Estimating Q^2 with the expectation value of the χ^2 distribution $E(Q^2) = N - 2$ results in the error's standard deviation, which is normalized to the resolution in frequency $\Delta\omega$ of the discrete spectrum

$$\sigma_{\Delta\omega} = \frac{1}{\Delta\omega} \sqrt{\frac{1}{N-2} \cdot \sum_{i=1}^{N} [\omega_i - (u_x k_{x,i} + u_y k_{y,i})]^2} \tag{14}$$

where the normalized $\sigma_{\Delta\omega}$ is $\sigma_\omega/\Delta\omega$. The error of the determined velocity of encounter now can be assumed to be a 2-D random Gaussian probability function

$$p(\vec{u}_e) = \frac{1}{2\pi\sqrt{\det(D^{-1})}} e^{-(1/2)(\vec{u}_{e,T} - \vec{u}_e)^t \cdot D \cdot (\vec{u}_{e,T} - \vec{u}_e)}. \tag{15}$$

A contour line of the 2-D probability function forms a confidence ellipse with the center $\vec{u}_e$ and the probability p that the "true" value $\vec{u}_{e,T}$ is included in the ellipse. The equation of the confidence ellipse is given by

$$\Delta(p) = (\vec{u}_{e,T} - \vec{u}_e)^t \cdot D \cdot (\vec{u}_{e,T} - \vec{u}_e) \tag{16}$$

or substituting the eigenvalues λ_1^2 and λ_2^2 and eigenvectors $\vec{w}_1$ and $\vec{w}_2$ of matrix D into (16)

$$\Delta(p) = \lambda_1^2 \cdot \left[\vec{w}_1^t \cdot (\vec{u}_{e,T} - \vec{u}_e)\right]^2 + \lambda_2^2 \cdot \left[\vec{w}_2^t \cdot (\vec{u}_{e,T} - \vec{u}_e)\right]^2. \tag{17}$$

The lengths of the confidence ellipse's half axes a and b are

$$a = \frac{\sqrt{\Delta(p)}}{\lambda_1} \quad \text{and} \quad b = \frac{\sqrt{\Delta(p)}}{\lambda_2}. \tag{18}$$

The orientation angle θ of the confidence ellipse is given by

$$\theta = \operatorname{atan}(\vec{w}_1) \quad \text{or} \quad \theta = \operatorname{atan}(\vec{w}_2) - \frac{\pi}{2}. \tag{19}$$

The scaling factor $\Delta(p = 0.683)$ is 2.3 for a 68.3% confidence ellipse. A detailed derivation of the error model's concept can be found in [14].

D. Consideration of Higher Harmonics and Aliasing

The first version of the algorithm to determine the velocity of encounter considered the spectral sea-state energy localized on the dispersion relation following (4). It became apparent that the number of regression coordinates could be increased by orders of magnitude if the higher harmonic signals and the signals that are folded by temporal aliasing are also considered for the least-squares method.

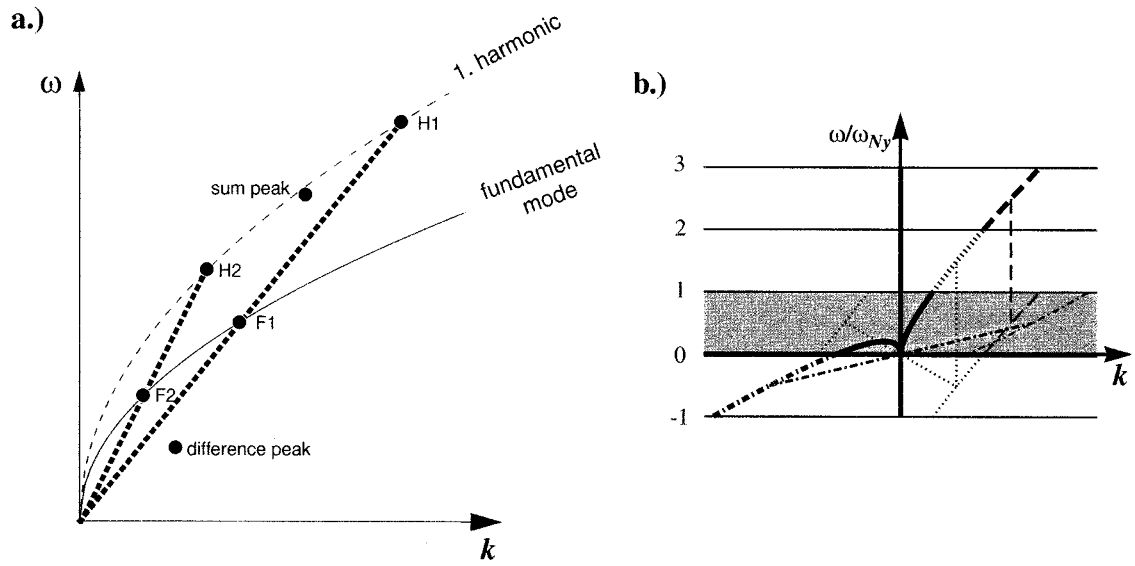

Fig. 3. Spectral nonlinearities and aliasing. (a) In a $k-\omega$-slice, the fundamental mode dispersion relation is given (solid line). Choosing two spectral wave components (F1 and F2) allows a vector construction of nonlinear quadratic interactions: $2\cdot F1 = H1$, $2\cdot F2 = H2$, $F1+F2 =$ sum peak, and $F1-F2 =$ difference peak. The nonlinearities $H1$, $H2$ are located on the dispersion relation of the first order $p=1$. The first-order dispersion relation (dashed line) locates additional spectral signal used to increase the accuracy of the algorithm. (b) The spectral representation of temporal undersampling due to a slow-rotating nautical radar antenna is given (thin lines). Applying spectral symmetries as a method to reconstruct the signal enables the Nyquist limit to be overcome (thick lines).

1) Higher Harmonics: One source of additional spectral signal structures in the spectrum $P(k_x, k_y, \omega)$ are the higher harmonics. The reasons for the appearance of higher harmonics are the nonlinearity of the imaging of the sea state by a nautical radar and the relatively weak nonlinearity of the sea-surface waves themselves. The nonlinearity of the radar's ITF is caused mainly by shadowing effects, since a nautical radar works at grazing incidence angles. The following equation of the harmonic dispersion relation of the order p results by scaling (4) with the factor $p+1$ ($p=0$ for the "fundamental mode" dispersion relation $\omega = \mathcal{S}_0^{\pm}(\vec{k}, \vec{u}_e)$

$$\mathcal{S}_p^{\pm} = \pm(p+1)\sqrt{\frac{gk}{p+1}\tanh\left(\frac{kh}{p+1}\right)} + \vec{k}\cdot\vec{u}_e. \tag{20}$$

A schematic diagram of the first-order nonlinear structures is given in Fig. 3(a). Regression coordinates found in nonlinear dispersion relations apart from the fundamental mode are also used to increase the accuracy of the algorithm.

2) Aliasing in the Three-Dimensional (3-D) Spectrum: Aliasing occurs if a signal of a certain wavelength or certain wave period is spatially or temporally undersampled. Due to the relatively slow repetition time T_r of a nautical radar antenna, signals that have a shorter period than 2 T_r are temporally undersampled. The repetition time T_r normally is of the order of 2 s.

In the spectrum $P(k_x, k_y, \omega)$, two symmetry conditions of the FFT are used to reconstruct signals, which are temporally undersampled: 1) the $2\omega_{Ny}$ periodicity (here the Nyquist frequency ω_{Ny}) is given by π/T_r)

$$P(k_x, k_y, \omega) = P(k_x, k_y, \omega + n\omega_{Ny}) \tag{21}$$

and 2) the point symmetry to the point of origin $P(k_x=0, k_y=0, \omega=0)$

$$P(k_x, k_y, \omega) = P(-k_x, -k_y, -\omega) \tag{22}$$

here n is an integer used to index the intervals $[n\omega_{Ny}; (n+1)\omega_{Ny}[$. The reconstruction of aliased dispersion shells (see Fig. 3(b) for the reconstruction scheme) to overcome the Nyquist limit is described in detail in [8] and [15].

III. Current Regression Algorithm

The current regression algorithm is based on a two-step procedure. It starts with a rough first guess estimation of the current vector, taking into account the fundamental mode dispersion relation. After the first guess estimation of the current velocity, the spectral coordinates of the fundamental mode, the harmonics (20) and their aliased dispersion shells reconstructed with (21) and (22) are included in the regression algorithm, thus increasing the accuracy of the method. The implemented algorithm is restricted to the fundamental and first harmonic mode because the spectral energy of higher harmonics is very low.

A. First Guess

The first guess estimation of the current velocity is based on the assumption that the spectral coordinates ω_i on the fundamental mode $\mathcal{S}_0(\vec{k}_i)$ are discriminated by a spectral-energy threshold C_{FG} from the nonlinearities, the aliases, and the background-noise component. The spectral peak is assumed to be located in the frequency interval

$$\mathcal{A}_0 = [0, \omega_{Ny}]. \tag{23}$$

The spectral energy of the signal's aliased high-frequency part of the signal is below C_{FG}. The least-squares algorithm (7) and

(10) and the error model (18) and (19) are carried out if a sufficiently high number of regression coordinates (at least of the order of ten) is selected.

B. Iterations

The iterative part of the least-squares algorithm starts with the collection of the spectral coordinates whose energy exceeds a much lower spectral-energy threshold C_{IT} than C_{FG}. C_{IT} should discriminate the background-noise component from the Doppler-shifted spectral signal. Next, the frequency $\mathcal{S}_1^+(\vec{k}_i)$, in relation to the wavenumber $\vec{k}_i$, is calculated according to (20).

The Doppler term is estimated with the current value $\vec{u}_{j-1}$ of the previous iteration step $j-1$ or of the first guess. The estimated frequency is assigned to the interval

$$\mathcal{A}_n = [n \cdot \omega_{Ny}, (n+1) \cdot \omega_{Ny}] \tag{24}$$

multiplied by the (positive or negative) integer n and by the Nyquist frequency ω_{Ny}. If the frequency $\omega_p(\vec{k}_i)$ is located in the interval $\mathcal{A}_n$ with an even integer n, the frequency is shifted to the interval $\mathcal{A}_0$, and the $2\omega_{Ny}$ periodicity (21) is applied

$$S_{p,n}\left(\vec{k}_i\right) = \mathcal{S}_{p,n}\left(\vec{k}_i\right) - n \cdot \omega_{Ny}. \tag{25}$$

If the integer n is odd, the spectral coordinate $(\vec{k}_i, \mathcal{S}_{p,n}(\vec{k}_i))$ is mapped to the coordinate $(-\vec{k}_i, -\mathcal{S}_{p,n}(-\vec{k}_i))$ according to the point symmetry to the origin (22). The coordinate $(-\vec{k}_i, \mathcal{S}_{p,n}(-\vec{k}_i))$ is located in the frequency interval $\mathcal{A}_{-n-1}$. This spectral coordinate is shifted to the interval $\mathcal{A}_0$ by applying the $2\omega_{Ny}$ periodicity (21)

$$S_{p,n}\left(-\vec{k}_i\right) = -\mathcal{S}_p\left(-\vec{k}_i\right) + (n+1) \cdot \omega_{Ny}. \tag{26}$$

The model p, n, where p is the harmonic order, and n the indicator of the Nyquist interval, with the minimal distance $\mathrm{MIN}(|\omega_i - \mathcal{S}_{p,n}(\vec{k}_i)|)$ is used for the linear regression if this magnitude is less than a frequency difference value $\mathcal{C}_\delta \cdot \Delta\omega$. Therefore, for the iteration steps, (7) becomes

$$Q^2 = \sum_{i=1}^{N} \left(\frac{\mathrm{MIN}_{p,n}\left(\left|\omega_i - \mathcal{S}_{p,n}\left(\vec{k}_i\right)\right|\right)}{\sigma_\omega} \right)^2 \Rightarrow \mathrm{MIN} \tag{27}$$

now extended by a dispersion-model selection. The data sets have been processed with the frequency distance criterion $\mathcal{C}_\delta = 1$. This value takes into account only the finite frequency resolution.

IV. Analytical Interpretation

The error model was introduced in Section II-C. The results of the error model are dependent on the spectral distribution of the regression coordinates selected for the algorithm in Section III. Here the variation of the spectral distribution of the regression coordinates will be examined using simple scaling arguments.

A. Variation of the Measurement Duration

If the measurement duration T is changed by changing the number of sampled images or by changing the antenna rotation time T_r, the frequency resolution $\Delta\omega$ will vary. The frequency resolution also is the minimal Doppler frequency $\omega_D = \vec{k} \cdot \vec{u}_e$, which can be resolved. Therefore, the resolution at which the velocity of encounter $\vec{u}_e$ can be determined is directly proportional to $\Delta\omega$, i.e., T^{-1}. If one scales the measurement duration T by $\acute{T} = cT$, it follows that $\acute{\sigma}_{\Delta\omega} = c^{-1}\sigma_{\Delta\omega}$. Thus, the half axes a and b of the confidence ellipse are scaled by

$$\acute{a} = c^{-1}a \quad \text{and} \quad \acute{b} = c^{-1}b. \tag{28}$$

This means that, for example, a doubling of the measurement duration T leads to a halfing of the expected error.

B. Variation of the Spatial Dimensions

The spatial extension of an image is given by X and Y. The following remarks are valid for a large number of regression coordinates N. A local spectral change of N is then proportional to a change of the spectral point density $\rho = \Delta N \Delta k_x^{-1} \Delta k_y^{-1}$ of the regression coordinates. Following this, it is presumed that a variation of X or Y is directly proportional to N. Let c be a scaling constant for $\acute{N} = cN$. Here, N is the initial number of regression coordinates for X or Y, and $\acute{N}$ is the scaled number of regression coordinates for $\acute{X}$ or $\acute{Y}$. Using this relation for matrix D of (10), all of the coefficients in (12) are multiplied by c, and $\acute{D} = cD$ holds. For the lengths of the half axes of the error model's confidence ellipse [see (18)], it follows that

$$\acute{a} = \frac{\sqrt{\Delta}}{\sqrt{c}\lambda_1} \quad \text{and} \quad \acute{b} = \frac{\sqrt{\Delta}}{\sqrt{c}\lambda_2}. \tag{29}$$

Consequently, the lengths of the half axes (i.e., the error) are proportional to $c^{-(1/2)}$. Introducing two separate constants $\acute{X} = c_x X$, $\acute{Y} = c_y Y$ gives $(c_x c_y)^{-(1/2)}$.

C. Variation of the Peak Wavenumber

Let $\acute{k}_x$ and $\acute{k}_y$ be scaled wavenumbers of the regression coordinates scaled by the relations $\acute{k}_x = ck_x$ and $\acute{k}_y = ck_y$. Substituting these into (10), the scaled matrix $\acute{D}$ is given by $\acute{D} = c^2 D$. Then, the lengths of the confidence ellipse become

$$\acute{a} = \frac{\sqrt{\Delta}}{c\lambda_1} \quad \text{and} \quad \acute{b} = \frac{\sqrt{\Delta}}{c\lambda_2}. \tag{30}$$

Therefore, the lengths of the half axes with varying wavenumber k are proportional to c^{-1}. For wave regimes mainly consisting of long waves (e.g., swell), poorer results are expected than for regimes consisting of waves of small wavelengths (e.g., wind sea).

D. Variation of the Directional Spread

Just as the component of the velocity of encounter $\vec{u}_e$ parallel to the wave's travel direction is shifted in frequency, the spectral directional distribution (i.e., the directional spread) is important for the accuracy of the determination of the $\vec{u}_e$ component directed perpendicular to the mean wave travel direction.

The effective influence of the directional spread is shown by using a spectrum symmetric to the k_y axis as an example. In this case, it follows directly that the coefficients D_{xy} and D_{yx} in (10) disappear. The directional spread is varied by multiplying the k_x component of the regression coordinates by the factor c. The scaled matrix $\acute{D}$ is therefore given by

$$\acute{D} = \begin{pmatrix} c^2 D_{xx} & 0 \\ 0 & D_{yy} \end{pmatrix}. \tag{31}$$

The eigenvalues are

$$\lambda_{1,2}^2 = \frac{c^2 D_{xx} + D_{yy}}{2} \pm \frac{|c^2 D_{xx} - D_{yy}|}{2}. \tag{32}$$

From (32) and (10), it follows that

$$\frac{a}{b} = c\sqrt{\frac{D_{xx}}{D_{yy}}}. \tag{33}$$

The half axis a (giving the error of the u_y component) and the coefficient D_{xx} are assumed to be constant. The half axis b is then proportional to c^{-1}. The broader the directional spread perpendicular to the mean wave travel direction is, the more accurate the calculated perpendicular component of $\vec{u}_e$ will be.

E. Extension of the Stewart and Joy-Weighting Function

With (2), the definition of $\vec{u}_e$ for a single wave was introduced by Young *et al.* [12]. The spectral regression coordinates of the least-squares algorithm originate from a wave field assumed to be a superposition of waves. Let us assume a spectrum $P(k_x, k_y, \omega)$ of a wave field that consists of a set K of wavenumbers $\vec{k}_i$ with $i = 1, \cdots, N$ belonging to the coordinates selected by the algorithm's last iteration step (see Section III-B). A weighting function is introduced extending (2), which is for a single wave k to an expression which is for a set K of waves

$$\vec{u}_e(z, K) = \frac{1}{\underbrace{\det\begin{pmatrix} \sum_{i=1}^{N} k_{x,i}^2 & \sum_{i=1}^{N} k_{x,i}k_{y,i} \\ \sum_{i=1}^{N} k_{y,i}k_{x,i} & \sum_{i=1}^{N} k_{y,i}^2 \end{pmatrix}}_{\sigma_\omega^{-2} D}} \sum_{i=1}^{N} \cdot \left[\underbrace{\begin{pmatrix} k_{x,i}^2 & k_{x,i}k_{y,i} \\ k_{y,i}k_{x,i} & k_{y,i}^2 \end{pmatrix}}_{\sigma_\omega^{-2} D_i} \underbrace{2k_i \int_{-d}^{0} \vec{u}(k) e^{(2k_i z)}\, dz}_{\vec{u}_e(z,k)} \right] \tag{34}$$

or in its abbreviated form

$$\vec{u}_e(z, K) = \frac{\sum_{i=1}^{N} [D_i \vec{u}_e(z, k)]}{\det(D)} \tag{35}$$

where

D — matrix of (10) and (11);

D_i — ith element of D;

$\vec{u}_e(k_i)$ — ith current vector of encounter, calculated using (2).

The sum $\sum_{i=1}^{N}$ is substituted by $\int_k dk$ when considering a continuous spectrum. In order to consider the impact of the Doppler term of (4) $\vec{k}_i \cdot \vec{u}$ for i waves, the matrix form has been chosen. It is obvious from (34) that the velocity vector of encounter $\vec{u}_e(z, K)$ is quadratically weighted with k and waves traveling perpendicularly to the current direction do not contribute.

V. Analysis of Simulated and Measured Image Sequences

Data sets were generated by a numerical model to investigate the algorithm outlined in Section III under controlled conditions. A description of the data sets and the presentation of the algorithm's results will be given in Section V-A. Data sets obtained from measurements and their interpretation will be presented in Sections V-B and V-C.

A. Monte Carlo Simulations

A numerical model to simulate image sequences of the sea surface and the imaging by nautical radars has been implemented at GKSS Research Center, Geesthacht, Germany, in cooperation with Clima Maritimo, Madrid, Spain [16]. The algorithm to determine the velocity of the encounter has been applied to these image sequences to test the behavior of the algorithm with regard to external hydrographic parameters. The parameters used to calculate the image sequences are the spatial and temporal dimensions, the frequency spectrum (JONSWAP in this examination), the directional spread (MITSUYASU in this examination), the water depth, and the velocity of encounter. The input parameters are listed in Table I. The specific parameters of this work are listed in Table II. Initially, the discrete grid points for the spatial and temporal coordinates are set by a simulation software. The elevation of the water surface is processed for each spatial grid point. The amplitudes of the waves are calculated with a Rayleigh probability distribution. The wave's first time step is realized by calculating a random phase. During subsequent time steps, the waves propagate according to the linear dispersion relation (6). An example of a simulated sea surface is shown in Fig. 4(a). The radar images are calculated based on geometrical optics. An image of a binary shadow mask is calculated by geometrical optics [Fig. 4(b)]. On a combination of the shadow mask and a surface modulated by the surface tilt is shown in Fig. 4(c). Speckle is not included in the simulated image sequences, and thus the SNR is much higher than those for real measurements.

1) Statistical Test of the Error Model: To prove the statistical significance of the error model described in Section II-C, an ensemble of 50 deterministic realizations (i.e., 50 sea-surface sequences) of a stochastically equivalent situation were calculated by random variation of the phases and the amplitudes. Parameter set 1 of Table II was chosen. A set of 50 current components $(u_x, u_y)_i$ and the accompanying confidence ellipse values were calculated for these 50 realizations.

The model's input current vector (u_x, u_y) is (1.5, 0.0) ms^{-1}. The mean value for all 50 current components for the first guess iteration step is (1.487, 0.073) ms^{-1}. After ten iteration steps, a value of (1.505, −0.001) ms^{-1} is obtained. The increase of

TABLE I
INPUT PARAMETERS OF THE SIMULATION SOFTWARE

grid size	Δx, Δy, Δt
numbers of grid points	N_x, N_y, N_t
wind sea spectrum	
JONSWAP	
fetch	F
wind speed	U_{10}
PIERSON-MOSKOWITZ	
significant wave height	Hs
directional distribution	
MITSUYASU	
mean wave travel direction	θ_p
statistics	
phase	[eq. distr.| 0]
spectral power	[const. | χ_2^2]
water depth	h
current velocity	
absolute value	u_c
direction	θ_c
antenna	
antenna height	H
distance antenna - image center	X, Y
models	
sea-surface elevation	
shadow mask	
tilt-shadow mask	

TABLE II
PARAMETER SETTINGS OF SIMULATIONS

parameter	set 1	set 2
number of images	32	32
antenna rotation time	2.57 s	2.65 s
grid size Δx	7.5 m	9.3 m
grid size Δy	7.5 m	9.3 m
antenna height	12.5 m	12.5 m
distance antenna - image center	780 m	1000 m
number of grid points (x-direction)	128	128
number of grid points (y-direction)	128	128
incidence angle (begin of image)	2.4°	1.8°
incidence angle (center of image)	0.9°	0.7°
incidence angle (end of image)	0.6°	0.5°
JONSWAP- (1) or P.-M.-Spectrum (2)	(2)	(1)
threshold C_{FG} (first guess)	0.2	0.2
threshold C_{IT} (iterations)	0.02	0.02

accuracy of the algorithm is shown by comparing the first guess and the last iteration step, as shown in Fig. 5.

The histograms for the first guess and the last iteration step of the number of the collected regression coordinates N, the error's standard deviation $\sigma_{\Delta\omega}$, and, as an example, the half axis a of the confidence ellipses (the histogram of half axis b has the same qualitative behavior) is shown in Fig. 6.

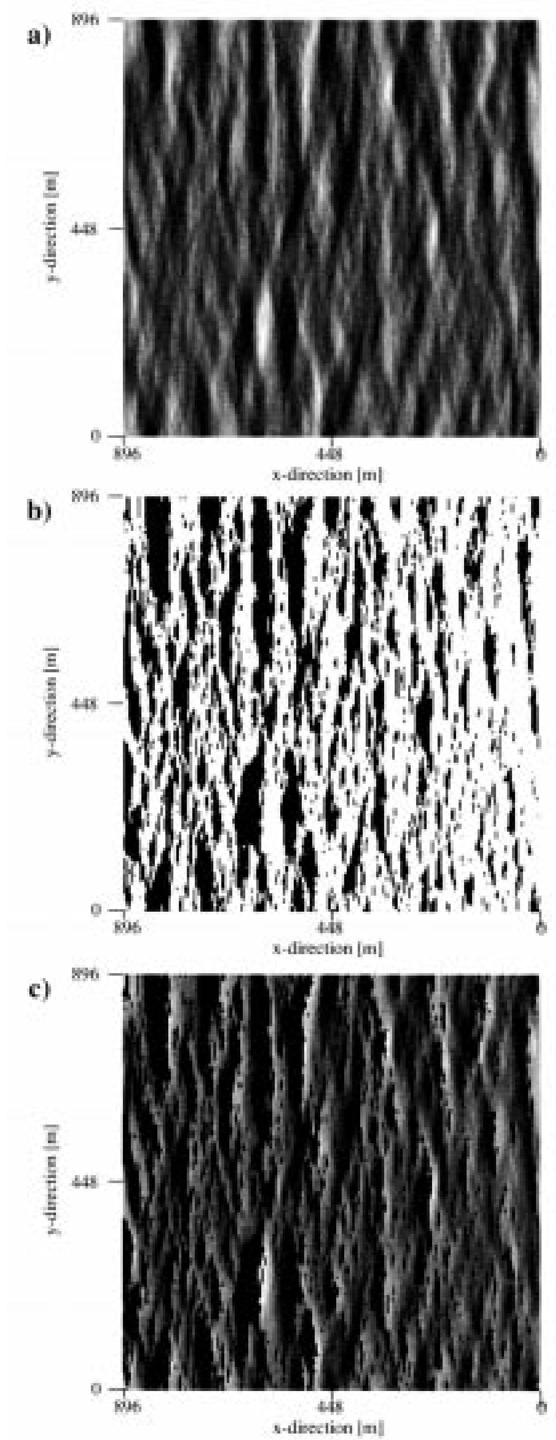

Fig. 4. Examples of images of (a) a simulated sea state, (b) the shadow-mask calculated by geometrical optics, and (c) the simulation of a radar image that is the multiplication of the shadow mask with the tilt modulation mask.

The histograms over N show the significant increase of collected regression coordinates. This increase can be explained by the decrease of the spectral-energy threshold C_{IT} value of the iterations and by considering the higher harmonics and aliases. The increase of the mean value $\overline{N}$ by a factor of 14.5 leads

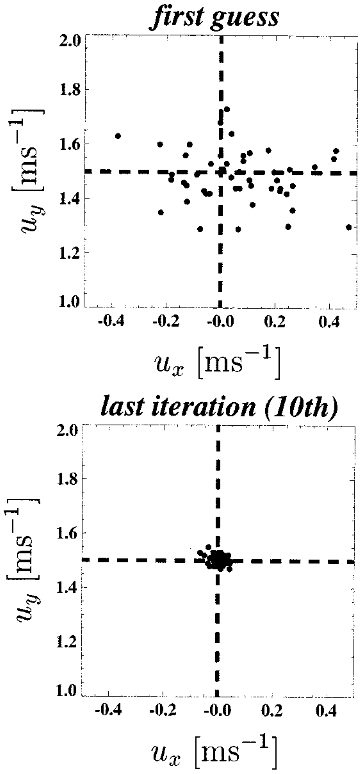

Fig. 5. Accuracy of the LSM. The calculated velocity vectors of 50 realizations are given as points in the two-dimensional (2-D) velocity plane. The upper diagram shows the results of the first guess, and the lower diagram shows the results of the last iteration step.

directly to an increase of the accuracy of the algorithm by a factor of 3.8 [see also (29)]. The histograms over the error's standard deviation $\sigma_{\Delta\omega}$ indicate a narrow-banded convergence to the value of $\sigma_{\Delta\omega} = 0.39$. The existence of values which differ strongly from this value is an indication that the algorithm fails for those cases.

The histogram over the half axis a shows a strong narrowing to a significantly lower value (i.e., higher accuracy) of a for the last iteration step. The statistical significance of a single measurement is therefore much higher.

2) Variation of the Directional Spread: The directional spread of a given spectrum strongly influences the accuracy of the result (see Section IV-D). In the simulation, the directional spreading function following a Mitsuyasu distribution was varied artificially by scaling the spreading parameter s with fixed factors c = 1, 10, 20, and 30. Here, c = 1 denotes the normal Mitsuaysu distribution and higher values of c lead to a narrowing of the directional spread. An ensemble of 15 realizations was calculated for each of the cases c = 1, 10, 20, and 30. The results for the half axes a and b are given in Fig. 7. For the half axis a, which gives the error in the mean wave travel direction, no significant change with c is observed. For the half axis b, which gives the error normal to the wave travel direction, an increase of the error with the narrowing of the directional distribution is obvious. The results of the numerical simulations and those from the analytical examination [see Section IV-D] agree qualitatively.

3) Variation of Mean Wave Travel Direction: A series of simulations of parameter set 1 in Table II was calculated for directions between the current vector and the mean wave travel direction of 0°, 30°, 60°, and 90°. For each of these directions, an ensemble of 15 realizations was calculated. The algorithm was applied 1) to the sea state spectrum and 2) the shadow mask of the same realizations representing the case of an extreme radar ITF, resulting in a strong effect of the ITF. Furthermore, the ensembles were calculated from directional spectra with a narrow spread, for which the effect of the directional change can be seen more clearly. Fig. 8 shows the spectral distribution.

In Fig. 9(a), one can see that the change of mean wave travel direction directly leads to a rotation of the confidence ellipses. Other effects such as a change in the sizes of the half axes are not significant. The rotation of the confidence ellipses can also be seen in the results calculated from the shadow-mask spectra given in Fig. 9(b), but there is a strong effect on the sizes of the confidence-ellipse half axes. This change in the quantitative properties of the confidence ellipses becomes more clear if one regards the shape of the integrated wavenumber spectra. There is no change of the spectral shape when there is a directional change (see Fig. 8, left). However, due to the directional dependence of the ITF of the shadow mask, the change of direction leads to a completely different shape of the spectra. The directional spread of the image spectrum is dependent on the mean wave travel direction because of the azimuthal dependency of the geometrical shadowing (see [17]).

4) Variation of the Velocity of Encounter: One simulation with parameter set 2 in Table II for each interval of 1 ms^{-1} was calculated for a range in the velocity of encounter between (u_x, u_y) = (0.0, 0.0) ms^{-1} and (0.0, −16.0) ms^{-1}. Not all results of the algorithm are reasonable when using the fundamental dispersion shell given in (4) as the model function for the first guess. Looking at Fig. 10 of $\sigma_{\Delta\omega}$ [see (14)], one can see that for all results lower than $u_y = -6$ ms^{-1} the least-squares algorithm has failed. The reason for the failure is the misinterpretation of aliased spectral energy belonging to the fundamental mode in the first guess. Fitting the wrong dispersion model leads to high values of $\sigma_{\Delta\omega}$.

When extending the algorithm by calculating all dispersion models of the fundamental mode, by including the aliased models, and $\sigma_{\Delta\omega}$, a decision can be made as to which of the models (whether the fundamental-mode model or its aliased model) the collected energy belongs. This is visualized in Fig. 10. Here $\sigma_{\Delta\omega}$ of the fundamental mode (solid line) and the first aliased (aliased from the interval $\omega_{Ny} \leq \omega \leq 2\omega_{Ny}$, dotted line) are given. Reasonable results are given for $u_y = 0, \cdots, -6$ ms^{-1}. For higher values of u_y, the fundamental-mode model's $\sigma_{\Delta\omega}$ indicates a failure due to a misinterpertation. Between $u_y = -11$ *and* -13 ms^{-1}, the aliased model yields reasonable results.

The velocity ranges marked by the very high values of $\sigma_{\Delta\omega}$ indicate the transition zone where the sea-state energy is located close to the Nyquist frequency. Here, the low-frequency part of the spectrum is not aliased but the spectral high-frequency tail already is aliased and therefore backfolded. This leads to a misinterpretation resulting in the very high values of $\sigma_{\Delta\omega}$ for both models.

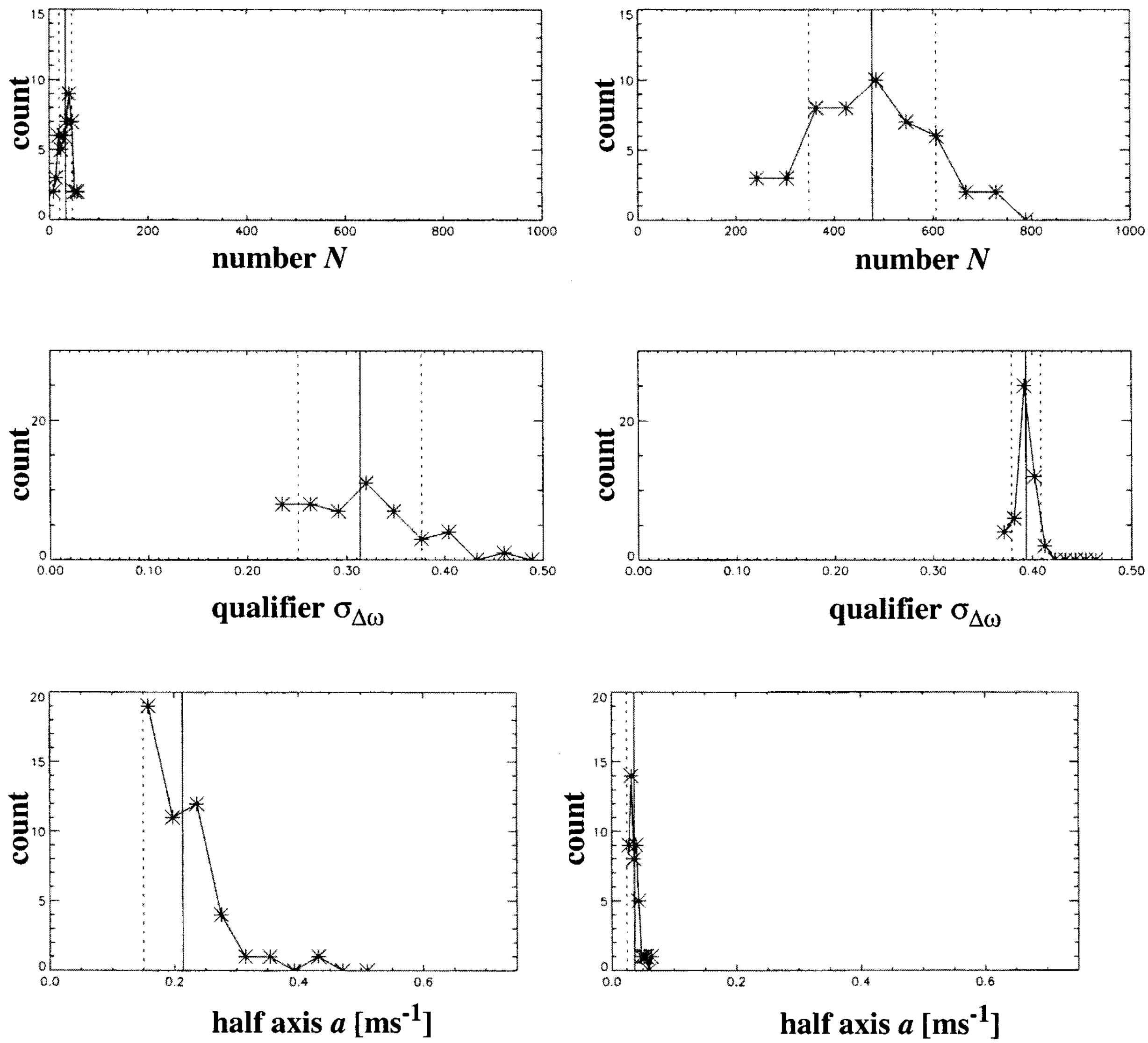

Fig. 6. (Top) Histograms over the number N of regression coordinates of 50 realizations. (Middle) Histograms over the error's standard deviation $\sigma_{\Delta\omega}$. (Bottom) Over the confidence-ellipse half axis a. The left column denotes the first guess for all histograms and the right column denotes the last iteration.

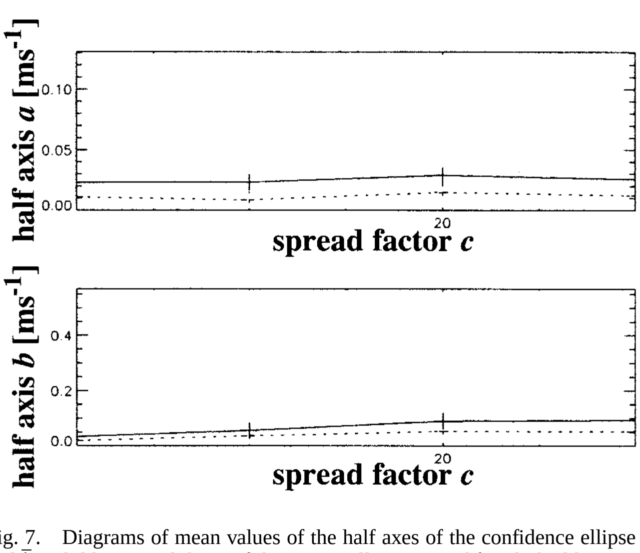

Fig. 7. Diagrams of mean values of the half axes of the confidence ellipse $\overline{a}$ and $\overline{b}$ (solid lines) and those of the scatter ellipse a_s and b_s (dashed lines), all depending on the spread factor c.

B. Ship-Based Measurements

The data presented were taken aboard the R.V. Gauss (cruise no. 268). The cruise took place from November 24 to December 13, 1995 in the North Sea and the Norwegian Sea.

1) Description of Radar and Doppler Log Data: For comparision, Doppler Log (DOLOG) data are used. For this instrument, the principle of measurement is based on determination of the frequency shift between the transmitted and received acoustic ultrasonic signals. The DOLOG has two modes: the *bottom track* and the *water track*. In bottom-track mode, the sound wave is reflected at the bottom: the speed of the ship relative to the bottom is determined. In the water-track mode, the sound wave is reflected from suspended matter at a certain water depth defined by the time offset of the actual signal. The water track depth here is 40 m. The accuracy of the DOLOG aboard the R.V. GAUSS is 10^{-2} ms^{-1}.

The radar parameters 1) number of images, 2) antenna rotation time, 3) gridsizes, 4) antenna height, 5) numbers of grid

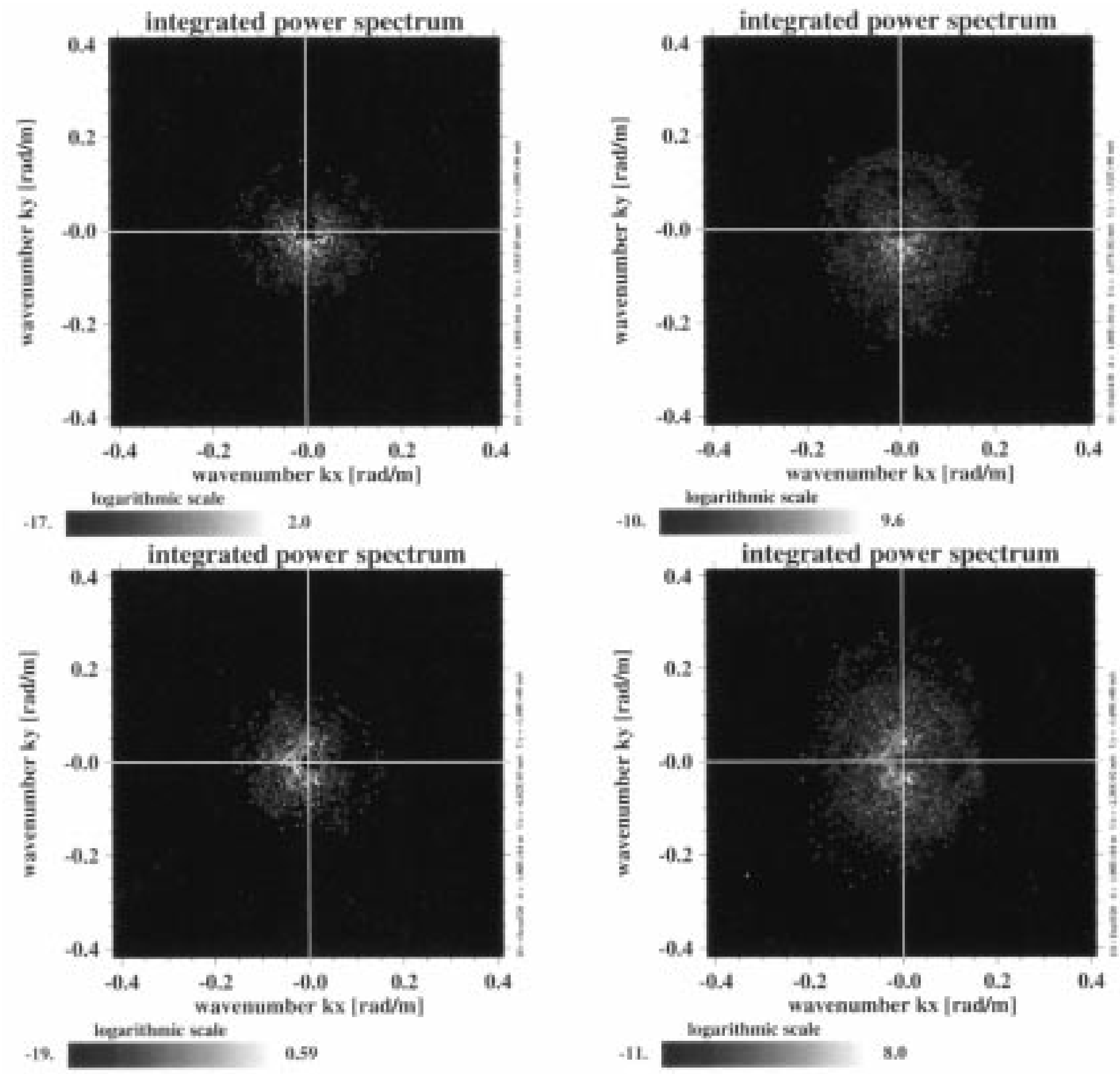

Fig. 8. Simulated wind-sea spectra for mean wave travel directions. (Top) 0° and (bottom) 90°. In the left column, the sea-state spectra are given and on the right side, the shadow-mask spectra are given.

points, and 6) thresholds were similar to the Table II parameter set 1 on cruise no. 268.

2) Measurement Results: For a sufficiently high number of 297 radar data sets, the current vectors of encounter were calculated and compared with the respective water-track DOLOG current vectors. In Fig. 11, the comparisons of the algorithm's first guess and last iteration step are given.

The scatter of the vector velocity difference $(u_x^{RADAR} - u_x^{DOLOG}, u_y^{RADAR} - u_y^{DOLOG})$ for the first guess (top) and the last iteration step (bottom) is given on the left side. The magnitude of scatter is given as a scatter ellipse, which includes 68.3% of all values. A significant decrease of scatter is obvious for the last iteration. This decrease is caused by the increase in the algorithm's accuracy due to the consideration of a higher number of spectral regression coordinates. That there still is a noticeable scatter for the last iteration is explained by the different measurement principles of the radar and DOLOG instruments: the DOLOG measures the velocity of the encounter based at a water depth of 40 m, whereas the radar measures specifically in the top layer of the ocean integrating over a huge measurement area. Because of these principal differences, a minor scatter cannot be expected. This hypothesis has been proved by [18].

On the right side around the same vector velocity differences the confidence ellipses, indicating the estimation of error calculated by the algorithm (see Section II-C), are given for the first guess and for the last iteration step. The confidence ellipses calculated by the algorithm decrease significantly from the first guess to the last iteration. The confidence ellipses for the last iteration are much smaller than the scatter explained by the principle differences in measurement. This fact predicts a higher accuracy unevaluated at the present time. Therefore, a future step must be a validation of the radar algorithm's data comparison with current meters resolving the vertical current profile (e.g., acoustic doppler current profiler).

C. Coastal-Based Measurements

In coastal waters, horizontal gradients of the tidal current are induced by the changing water depth. Static radar signatures are

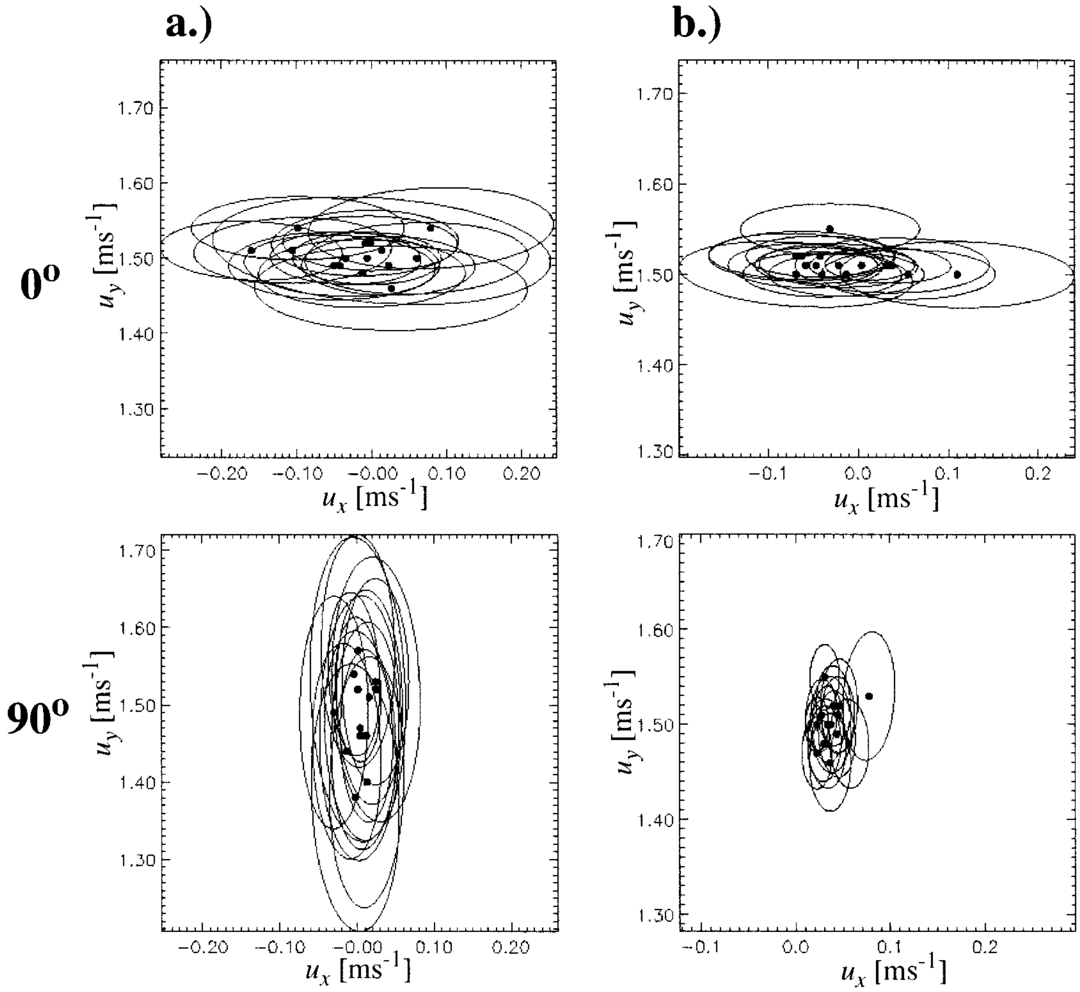

Fig. 9. Confidence ellipses for the mean wave travel directions. (Top) 0° and (bottom) 90° resulting from (a) sea-state spectra and (b) shadow-mask spectra.

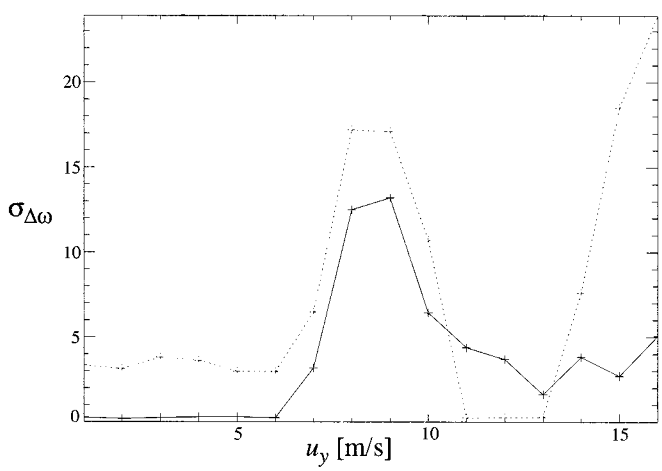

Fig. 10. First-guess error's standard deviation $\sigma_{\Delta\omega}$ versus the u_y component of the velocity of encounter. The fundamental mode (solid) and the aliased dispersion model (dotted; aliased from the interval $\omega_N y, \cdots, 2\omega_N y$).

generated by the hydrodynamic interaction of the small-scale surface roughness with the current gradients. The waves are refracted due to the inhomogeneities of the water depth and the tidal current.

1) Description of Radar Data: The data sets used for the analysis were taken by a nautical X-band radar mounted on the island of Sylt in the German Bight in the period from February to June 1997. Measurements were taken once an hour. One data set consists of 32 images from successive antenna rotations. The antenna rotation time N_t is 2.25 s. The images cover an area with a radius of 2 km. The observed area is of high interest since morphological changes that are likely to lead to changes of the flood stream situation have occurred in recent years and are still in progress. Measurements taken hourly on February 13 from 03:00 UTC to 16:00 UTC 1997 were analyzed for the tidal periodicity of the current velocity. The method presented here is based on the assumption of spatial homogeneity and temporal stationarity. The assumption of stationarity is not violated due the short duration of each measurement. However, most of the water surface scanned by the radar is inhomogeneous with varying water depth. A nearly homogeneous area 873 m × 873 m ($N_x = 128$, $N_y = 128$) in size and 1400 m west of the antenna was chosen for the analysis (Fig. 12). Except for the measurement taken at 11:00 UTC, the static radar signatures did not extend into the analysis area, indicating that the horizontal current gradients are small. The bathymetry was acquired by echo sounding during the period from July to September 1997. The water depth was corrected with a tidal gauge.

2) Measurement Results: The results produced by the regression algorithm, the calculated current vectors and error el-

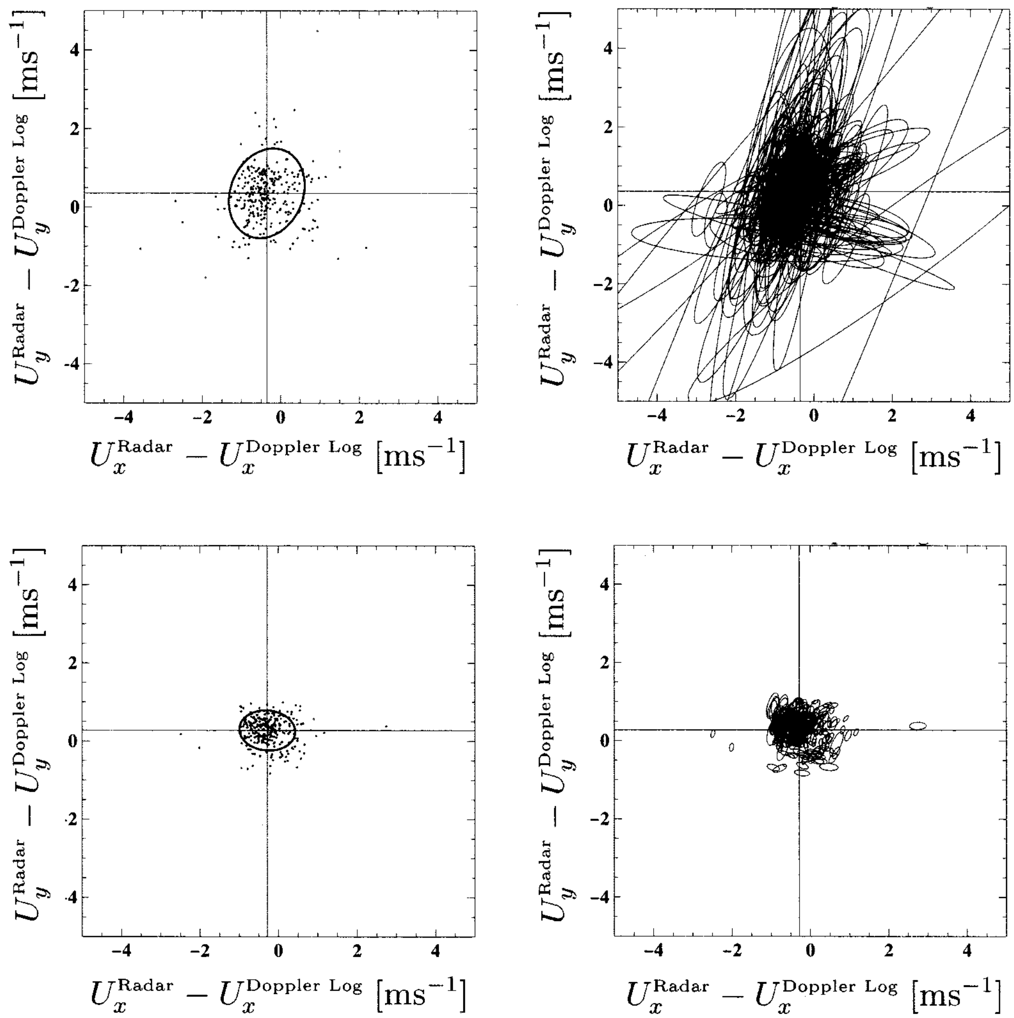

Fig. 11. (Left) Scatter and confidence ellipses around the (right) same scatter for (top) the first guess and (bottom) the last iteration step of the vector difference $(u_x^{RADAR} - u_x^{DOLOG}, u_y^{RADAR} - u_y^{DOLOG})$ given in the $\vec{u}$ plane.

lipses, together with the mean water depth of the analyzed area are outlined in Fig. 13. The current vector shows the temporal evolution as expected for the tidal influence. The length of the half axis perpendicular to the mean travel direction exceeds the length of the half axis parallel to the mean travel direction, especially for large regression errors, because the directional spread of the image spectrum is small. The error of the current estimation is large for a low water level and small for a high water level. This can be explained as follows: the signal-to-noise ratio of the image spectra over the analyzed tidal cycle is correlated with the water level. The current vector was estimated with the spectral-energy threshold of the iterations C_{IT} adapted automatically to the signal-to-noise ratio. The water level was highest (Fig. 13) at 05:00 UTC, and $N_{IT} = 132$ regression coordinates were collected with the threshold value $C_{IT} = 0.061$. At 12:00 UTC, the water level was lowest, and $N_{IT} = 52$ regression coordinates were selected with the threshold value $C_{IT} = 0.132$. The measurement at 11:00 UTC with the largest error ellipse is not reliable. The SNR was so low that the 15 spectral coordinates with the highest energy selected for the first guess already corresponded partially to the background-noise component, and thus the first guess failed. The result presented in Fig. 13 was obtained by setting $u_{FG} = 0$ m/s manually. During this measurement, a static radar signature extends beyond the analyzed area, indicating inhomogeneities of the tidal current. The measurements taken from a land-based station on the island of Sylt indicate the limitation of the method. The FFT implicitly assumes spatial homogeneity on a large scale. The extension of the current regression method to inhomogeneous areas requires the development of new algorithms for the estimation of the wavenumbers on a local spatial scale.

VI. Discussion

As it was made clear in the Sections IV and V-A, the LSM to determine the velocity of encounter from the wavenumber-frequency spectrum is directly dependent on the shape and the distribution of the spectral sea-state signal. The wider the signal's directional spreading, the more accurate the component of the current velocity perpendicular to the mean wave travel direction. Therefore, the quality of the measurements of the velocity of encounter and the following steps of the analysis are strongly

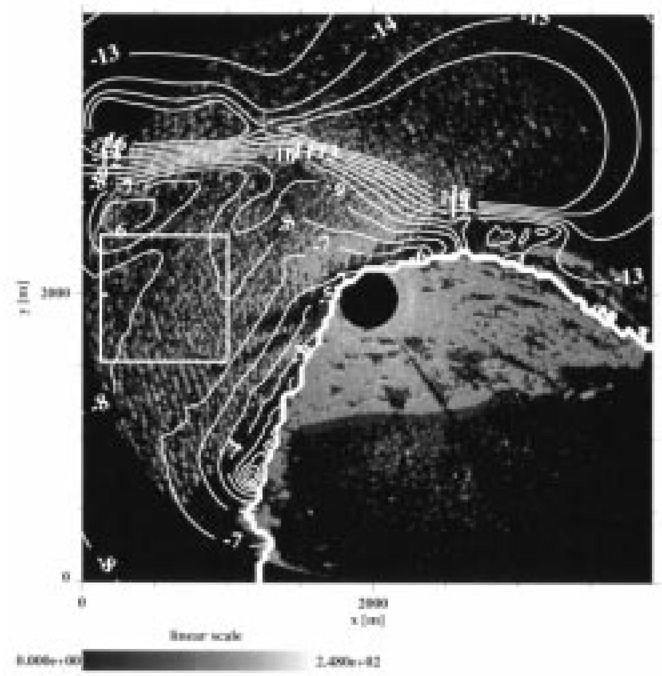

Fig. 12. Radar image of a sequence obtained from a land-based station on the island of Sylt in the German Bight on February 13, 1997, at 04:00 UTC. The square of 1400 m in width west of the antenna was chosen for the current estimation because this area is nearly homogeneous. The bathymetry was obtained from the Amt für Ländliche Räume (ALR).

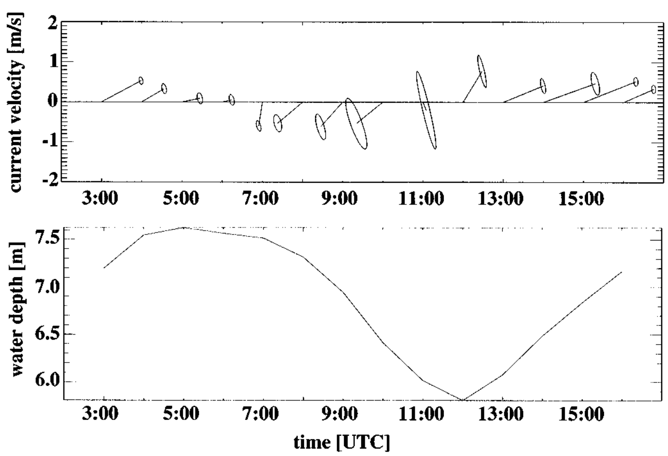

Fig. 13. Tidal cycle of the current velocity. (Top) Time series of the calculated current velocities and (bottom) error ellipses and water depth from a tidal gauge. The same scale is used for both components of the current velocity. The radar data sets were acquired on February 13, 1997 from a land-based station on the island of Sylt in the German Bight.

dependent on the actual sea state. As an example, the quality of the results is better for a well-developed wind sea than for swell during calm wind conditions, where the spectral distribution both in direction and in frequency is narrow. The error model (confidence ellipse and error's standard deviation) allows a quantification of the confidence.

The accuracy of the method is physically limited by the spectral frequency resolution for optimal cases and is on the order of 0.1 ms^{-1} to 0.2 ms^{-1} in the operational mode where 32 images are sampled by the nautical radar. This accuracy can be increased by a prolongation in time, and thus by collecting a higher number of images.

The accuracy is increased significantly by considering of the higher harmonic and aliased signals. Taking into account aliased signals allows utilization of the WaMoS II, even on fast cruising ships. In addition, the adaptation of the threshold to the SNR for the first guess and the iterations increased the reliability of the algorithm. The automatic adaption of the threshold calculates a constant spectral-energy threshold for the entire spectrum. As the 3-D image spectrum is folded by the low-pass filter impulse response function of the sensor, which lowers the spectral density for high wavenumbers, one comes to the conclusion that a constant threshold is not the proper quantity to separate signal from noise, especially for high wavenumbers. A task for the near future is the consideration of the spectral shape of the impulse response function. Two methods could be applied to obtain a threshold value depending on the wavenumber k. One method involves a 2-D fitting algorithm to parameterize the shape of the spectral background noise. A second alternative is to determine the spectral impulse response function by regarding the sensor's properties, such as spatial resolution, the shape of the transmitted electromagnetic field of the antenna, etc.

VII. Conclusions

A reasonable method to determine the velocity of encounter was developed. In combination with the implemented error model, the method is a convenient tool that is now in operational use. The analytical interpretations agree well with the Monte Carlo simulations and with the measurement results.

The limits of the presented method are the assumptions of homogeneity and stationarity of the sea state or the near-surface currents in the observed area. These limitations become critical, especially in coastal regions where processes such as wave refraction or diffraction and current gradients due to strong horizontal bathymetric gradients occur. To overcome this limitation, a method is under development that allows the determination of the near-surface current and other hydrographic parameters on a local spatial scale [17], [19]. Recent advances include the application of the presented method to optical image sequences acquired in hydraulic wave tanks for harbor or offshore planning purposes [20] or to determine the wind-drift velocity in wind-wave facilities [21].

Acknowledgment

The authors would like to thank Prof. Dr. J. Sündermann, Institute of Oceanography, Hamburg, Germany, Dr. W. Rosenthal, Dr. H. Günther, O. Outzen, H. Hatten, G. Schymura, GKSS Research Center, Geesthacht, Germany. Dr. J. C. Nieto Borge, Clima Maritimo, Ente Publico Puertos del Estado, Madrid, Spain, and J. Dittmer, Dittmer Oceanographic Instruments, Geesthacht, Germany. They also wish to thank the crew of the R.V. Gauss, especially Kpt. Walde and chief scientists D. Schrader, W. Schimmel, and A. Schulz, Bundesamt für Seeschiffahrt und Hydrographie, Hamburg, Germany, for providing the Doppler Log data sets. They would also like to thank the Amt für Ländliche Räume for the bathymetry data set for the Sylt measurements, and Prof. Dr. B. Jähne and his group, University of Heidelberg, Heidelberg, Germany, and Prof. Dr. W. Alpers, Dr. M. Gade, N. Braun, and Dr. P. Lange, University of Hamburg, Hamburg, Germany.

REFERENCES

[1] L. B. Wetzel, "Sea clutter," in *Radar Handbook*, 2nd ed, M. Skolnik, Ed. New York: McGraw-Hill, 1990, pp. 13.1–13.36.
[2] J. Dittmer, "Use of marine radars for real time wave field survey and speeding up transmission/processing," in *Proc. WMO/IOC Workshop on Operational Ocean Monitoring Using Surface Based Radars*, Geneva, Switzerland, 1995.
[3] F. Ziemer, "An instrument for the survey of the directionality of the ocean wave field," in *Proc. WMO/IOC Workshop on Operational Ocean Monitoring Using Surface Based Radars*, vol. 32, Geneva, Switzerland, 1995, pp. 81–87.
[4] K. Reichert, J. C. Nieto Borge, and J. Dittmer, "Wamos ii: An operational wave monitoring system," in *Proc. Oceanology Int.*, Brighton, U.K., 1998.
[5] K. Reichert, K. Hessner, J. C. Nieto Borge, and J. Dittmer, "Wamos ii: A radar based wave and current monitoring system," in *Proc. ISOPE'99*, vol. 3, Brest, France, 1999, pp. 139–143.
[6] J. W. Goodman, "Some fundamental properties of speckle," *J. Opt. Soc. Amer.*, vol. 66, pp. 1145–1150, 1976.
[7] F. Ziemer, "Directional spectra from shipboard navigation radar during lewex," in *Directional Ocean Wave Spectra*, R. C. Beal, Ed. Baltimore, MD: The Johns Hopkins Univ. Press, 1991, pp. 80–84.
[8] J. Seemann, F. Ziemer, and C. M. Senet, "A method for computing calibrated ocean wave spectra from measurements with a nautical x-band radar," in *Proc. Oceans '97 MTS/IEEE Conf., 500 Years of Ocean Exploration*, vol. 2, San Diego, CA, 1997, pp. 1148–1154.
[9] W. Alpers and K. Hasselmann, "Spectral signal to clutter and thermal noise properties of ocean wave imaging synthetic aperure radars," *Int. J. Remote Sensing*, vol. 3, pp. 423–446, 1982.
[10] J. C. Nieto Borge, "Overcome of the nyquist limit in frequency in nautical radar measurements of wave fields," in *Proc. 17th OMAE Conf.*, Lisboa, Portugal, 1998.
[11] H. Hatten, F. Ziemer, J. Seemann, and J. C. Nieto Borge, "Correlation between the spectral background noise of a nautical radar and the wind vector," in *Proc. 17th OMAE Conf.*, Lisboa, Portugal, 1998.
[12] I. R. Young, W. Rosenthal, and F. Ziemer, "A three-dimensional analysis of marine radar images for the determination of ocean wave directionality and surface currents," *J. Geophys. Res.*, vol. 90, no. C1, pp. 1049–1059, 1985.
[13] R. H. Stewart and J. W. Joy, "HF radio measurements of surface currents," *Deep Sea Res.*, vol. 21, pp. 1039–1049, 1974.
[14] J. Honerkamp, *Stochastic Dynamical Systems: Concepts, Numerical Methods, Data Analysis*. New York: VCH, 1994.
[15] J. C. Nieto Borge, "Significant wave height estimation from nautical radar data sets," Tech. Rep., GKSS Res. Center, Geesthacht, Germany, 1998.
[16] J. C. Nieto Borge and M. de Alfonso, "Methods of sea state simulation," External Rep., Dpto. Clima Marftimo, Ente Publico Puertos del Estado, Madrid, Spain, 1994.
[17] J. Seemann, C. M. Senet, H. Dankert, H. Hatten, and F. Ziemer, "Radar image sequence analysis of inhomogeneous water surfaces," in *Proc. 2nd Int. Symp. Operationalization of Remote Sensing, ITC*, 1999.
[18] ——, "An iterative technique to determine the near surface current velocity from time series of sea surface images," in *Proc. Oceans '97 MTS/IEEE Conf., 500 Years of Ocean Exploration*, vol. 1, 1997, pp. 66–72.
[19] C. M. Senet, J. Seemann, and F. Ziemer, "Hydrographic parameter maps deduced from ccd image sequences of the water surface supplemented by *in-situ* wave gauges," in *Proc. IEEE Int. Geoscience and Remote Sensing Symp.*, Honolulu, HI, 2000.
[20] C. M. Senet, J. Seemann, H. Dankert, J. R. Amoros Serret, J. C. Nieto Borge, and F. Ziemer, "Optical image sequence analysis and interpretation of the water surface in a multidirectional wave tank and its application in coastal engineering," in *Proc. 2nd Int. Symp. Operationalization of Remote Sensing, ITC*, Enschede, The Netherlands, 1999.
[21] C. M. Senet, N. Braun, P. A. Lange, J. Seemann, H. Dankertand, and F. Ziemer, "Image sequence analysis of water surface waves in a hydraulic wind wave tank," in *Int. Soc. Optical Engineering SPIE, Conf.: Applications of Digital Image Processing XXII*, vol. 3804, Denver, CO, 1999, pp. 148–158.

Christian M. Senet received the diploma degree from the University of Hamburg, Hamburg, Germany, in physical oceanography. He is currently pursuing the Ph.D. degree at the GKSS Research Center, Geesthacht, Germany.

He elaborated his diploma thesis ("Studies on Near-Surface Currents Measured with a Nautical Radar") at the GKSS Research Center in 1996.

Jörg Seemann received the diploma degree in 1993 from the Institute of Physics, University of Hamburg, Hamburg, Germany, having studied in the field of laser spectroscopy, and the Ph.D. degree from the Institute of Physical Oceanography, University of Hamburg, in 1997.

His Ph.D. dissertation focused on the analysis of radar image sequences of the oceans surface. Since 1997, he has worked on radar image sequence analysis of inhomogeneous water surfaces at GKSS Research Center, Geesthacht, Germany.

Friedwart Ziemer received the Ph.D. degree, writing his dissertation on wave measurements with nautical radars.

Since 1998, has been Head of the Department of Radar Hydrography, GKSS Research Center, Geesthacht, Germany. He has been with the Wave Research Group, since 1986. He is currently working on the development of incoherent and coherent nautical radars. The aim of the work is to obtain hydrographic maps especially, in coastal areas.